

The Strangest Proton?

Ferran Faura¹, Shayan Iranipour², Emanuele R. Nocera¹, Juan Rojo^{1,3},
and Maria Ubiali²

¹*Nikhef Theory Group, Science Park 105, 1098 XG Amsterdam, The Netherlands*

²*DAMTP, University of Cambridge, Wilberforce Road, Cambridge,
CB3 0WA, United Kingdom*

³*Department of Physics and Astronomy, VU, 1081 HV Amsterdam, The Netherlands*

Abstract

We present an improved determination of the strange quark and anti-quark parton distribution functions of the proton by means of a global QCD analysis that takes into account a comprehensive set of strangeness-sensitive measurements: charm-tagged cross sections for fixed-target neutrino-nucleus deep-inelastic scattering, and cross sections for inclusive gauge-boson production and W -boson production in association with light jets or charm quarks at hadron colliders. Our analysis is accurate to next-to-next-to-leading order in perturbative QCD where available, and specifically includes charm-quark mass corrections to neutrino-nucleus structure functions. We find that a good overall description of the input dataset can be achieved and that a strangeness moderately suppressed in comparison to the rest of the light sea quarks is strongly favored by the global analysis.

Contents

1	Introduction	2
2	Analysis settings	3
2.1	Experimental data	3
2.2	Theoretical calculations	4
2.2.1	The NOMAD ratio	4
2.2.2	Theoretical improvements	5
2.3	PDF sets	7
3	Results	8
3.1	Fit quality	8
3.2	Comparison with experimental data	9
3.3	Parton distributions	12
3.3.1	Comparison with NNPDF3.1	12
3.3.2	Total and valence strange distributions	14
3.3.3	Light quark, charm, and gluon PDFs	15
3.4	The strange content of the proton revisited	15
4	Summary	18

1 Introduction

An accurate determination of the strange quark and anti-quark parton distribution functions (PDFs) of the proton [1–3] is key to carrying out precision phenomenology at current and future colliders, specifically for measuring fundamental parameters of the Standard Model (SM) such as the mass of the W boson [4], the Weinberg angle [5], and electroweak parameters in general [6]. Because of the limited experimental information available, however, the strange quark and anti-quark PDFs remain much more uncertain than the up and down sea quark PDFs.

The strange quark and anti-quark PDFs have been determined from neutrino-nucleus deep-inelastic scattering (DIS) for a long time, specifically from measurements of dimuon cross sections, whereby the secondary muon originates from the decay of a charmed meson, $\nu_\mu + N \rightarrow \mu + c + X$ with $c \rightarrow D \rightarrow \mu + X$ [7–10]. When interpreted in terms of the ratio between strange and non-strange sea quark PDFs, $R_s \equiv (s + \bar{s})/(\bar{u} + \bar{d})$, these measurements favor values around $R_s \lesssim 0.5$ when PDFs are evaluated at values of the momentum fraction $x = 0.023$ and scale $Q = 1.6$ GeV. Therefore, it came as a surprise when a QCD analysis of the W - and Z -boson rapidity distributions measured by the ATLAS experiment in proton-proton collisions [11], later corroborated by an analysis based on an increased integrated luminosity [12], suggested instead a ratio closer to $R_s \simeq 1$. Complementary information on the strange quark and anti-quark PDFs is provided by W -boson production in association with light jets [13] and charm quarks [14], the latter process being dominated by the partonic scattering $g + s \rightarrow W + c$. Measurements of these processes were performed by the ATLAS [15, 16] and CMS [17, 18] experiments recently. Although ATLAS and CMS $W + c$ measurements turned out to be consistent at the parton level, different interpretations in terms of R_s were claimed [16, 17].

This state of affairs has motivated studies of the proton strangeness within the CT, MMHT, and NNPDF global fits, with overall consistent findings. The NNPDF3.1 analysis [19] found that, whereas the ATLAS W , Z dataset [12] does indeed favour a larger total strangeness, its χ^2 remains non-optimal when fitted together with the neutrino dimuon data. The recent CT18 global analysis [20] also presented fits with and without the

ATLAS measurement of [12], with the resulting PDFs differing by more than one-sigma both for the gluon and for the total strangeness. An update of the global PDF analysis from the MMHT collaboration [21], which for the first time accounted for the NNLO massive corrections to the neutrino dimuon cross-sections within a PDF fit, also revealed an enhanced strangeness driven by the ATLAS W , Z dataset. The resulting PDFs were however consistent within uncertainties with the corresponding fit once this dataset was excluded. Additional dedicated studies of the strange quark and anti-quark PDFs have been presented [22–26], however these focused on a restricted set of processes or datasets, or were based on theoretical and methodological assumptions that can potentially bias the results.

Given its phenomenological relevance for precision physics at the LHC, a global reinterpretation of all of the strangeness-sensitive measurements within an accurate theoretical and methodological framework appears to be therefore timely and compelling. This paper fulfills this purpose: we present an improved determination of the strange quark and anti-quark PDFs, accurate to next-to-next-to-leading order (NNLO) in perturbative QCD where available, by expanding the NNPDF3.1 analysis [19] in two respects. First, we take into account several new pieces of experimental information which are relevant to constrain the strange quark and anti-quark PDFs: charm-tagged to inclusive cross section ratios measured by the NOMAD experiment [10] in fixed-target neutrino-nucleus DIS; and an extended set of cross sections for inclusive gauge-boson production and W -boson production in association with light jets or charm quarks measured by the ATLAS [12, 15, 16] and CMS [17, 18] experiments in proton-proton collisions. Second, we improve the theoretical description of dimuon neutrino DIS structure functions, by implementing NNLO charm-quark mass corrections, and of $W+c$ production data, by including a theoretical uncertainty that accounts for the unknown NNLO QCD corrections; we also explicitly enforce the positivity of the F_2^c structure function.

The outline of this paper is as follows. In Sect. 2 we discuss the experimental data and the theoretical details used in this analysis, along with the PDF fits performed. In Sect. 3, we present the results of these fits, we assess their quality, and we use them to understand how the datasets and the theoretical framework affect the PDFs, in particular in relationship with the strangeness content of the proton. We finally provide a summary of our work in Sect. 4.

2 Analysis settings

In this section we present the experimental datasets used as input to our analysis, we then discuss the details of the corresponding theoretical computations, and we finally explain which PDF fits we perform to study their impact on the proton strangeness.

2.1 Experimental data

The bulk of the dataset included in our analysis corresponds to the one used in [27], which is in turn a variant of the dataset used in the NNPDF3.1 NNLO analysis [19]. It contains in particular measurements of the dimuon neutrino-nucleus DIS cross sections from the NuTeV experiment [9], and of inclusive gauge boson production in proton-(anti)proton collisions from several Tevatron and LHC experiments [12, 28–31]. These measurements represented the most constraining source of experimental information on the strange quark and anti-quark PDFs in the NNPDF3.1 analysis.

We supplement this dataset with a number of new measurements. Concerning neutrino-nucleus DIS, we include measurements of the ratio of dimuon to inclusive charged-current cross sections, $\mathcal{R}_{\mu\mu}(\omega) = \sigma_{\mu\mu}(\omega)/\sigma_{CC}(\omega)$, from the NOMAD experiment [10], see Sect. 2.2

for details. The data is presented for three kinematic variables ω : the neutrino beam energy E_ν , the momentum fraction x , and the square root of the final-state invariant mass $\sqrt{\hat{s}}$. Given that experimental correlations are not provided amongst measurements in different kinematic variables, only one measurement can be included in the fit at a time: we select the $n_{\text{dat}} = 19$ data points as a function of E_ν , the only variable which is directly measured by the experiment among the three. We will nevertheless verify that similar results can be obtained for instance with the $\sqrt{\hat{s}}$ -dependent dataset. The kinematic sensitivity of the NOMAD measurements is roughly $0.03 \lesssim x \lesssim 0.7$, as illustrated by the coverage of the x -dependent dataset.

Concerning proton-proton collisions, we augment the inclusive gauge boson production measurement from the ATLAS experiment at a center-of-mass energy (c.m.e.) of 7 TeV [12] with the off-peak and forward rapidity bins (not included in NNPDF3.1) for a total of $n_{\text{dat}} = 61$ data points. Furthermore we include the $n_{\text{dat}} = 37$ data points corresponding to the ATLAS (at a c.m.e. of 7 TeV) [16] and CMS (at a c.m.e. of 7 TeV and 13 TeV) [17, 18] $W+c$ measurements; for ATLAS, we consider the charm-jet dataset, which is amenable to fixed-order calculations (instead of the D -meson dataset). Finally we take into account the $n_{\text{dat}} = 32$ data points corresponding to the ATLAS W +jets measurement (at a c.m.e. of 8 TeV) differential in the transverse momentum of the W boson [15]. Overall, these LHC datasets are sensitive to the proton strangeness in the region $10^{-3} \lesssim x \lesssim 0.1$. The present analysis contains a total of $n_{\text{dat}} = 4096$ data points; experimental correlations within each dataset are available for all of the new measurements considered here and are therefore included in our analysis.

2.2 Theoretical calculations

The measurements outlined in the previous section correspond to hadronic observables already considered in [19], except for the ratio $\mathcal{R}_{\mu\mu}$ measured by the NOMAD experiment, and for the production of W bosons in association with light jets measured by the ATLAS experiment. Likewise, the theoretical settings adopted in the present analysis closely follow those described in the NNLO analysis of [19, 27] (whereby, in particular, the charm PDF is fitted), except for some improvements. In this section we discuss in turn the new NOMAD observable and the theoretical details unique to the present analysis.

2.2.1 The NOMAD ratio

As mentioned above, the NOMAD experiment measured the ratio of dimuon to inclusive charged-current cross sections, $\mathcal{R}_{\mu\mu}$. Both the numerator and the denominator of $\mathcal{R}_{\mu\mu}$ are evaluated as two-dimensional integrals of the differential cross sections over the fiducial phase space. For the E_ν -dependent data set, which we include by default, we have

$$\sigma_i(E_\nu) = \int_{x_0}^1 \frac{dx}{x} \int_{Q_{\min}^2}^{Q_{\max}^2(x)} dQ^2 \frac{d^2\sigma_i}{dx dQ^2}(x, Q^2, E_\nu), \quad (2.1)$$

where $Q_{\max}^2(x) = 2m_p E_\nu x$ and $x_0 = Q_{\min}^2/(2m_p E_\nu)$, with m_p the proton mass. While the NOMAD measurements are reconstructed for $Q^2 \geq 1 \text{ GeV}^2$, we assume $Q_{\min}^2 = Q_0^2$, where $Q_0 = 1.65 \text{ GeV}$ is the initial parametrization scale adopted in our analysis [19]. We explicitly verified that results are unaffected if $Q_{\min}^2 = 1 \text{ GeV}^2$ is chosen instead. The integrand in Eq. (2.1) is either the dimuon ($i = \mu\mu$, entering the numerator or $\mathcal{R}_{\mu\mu}$) or

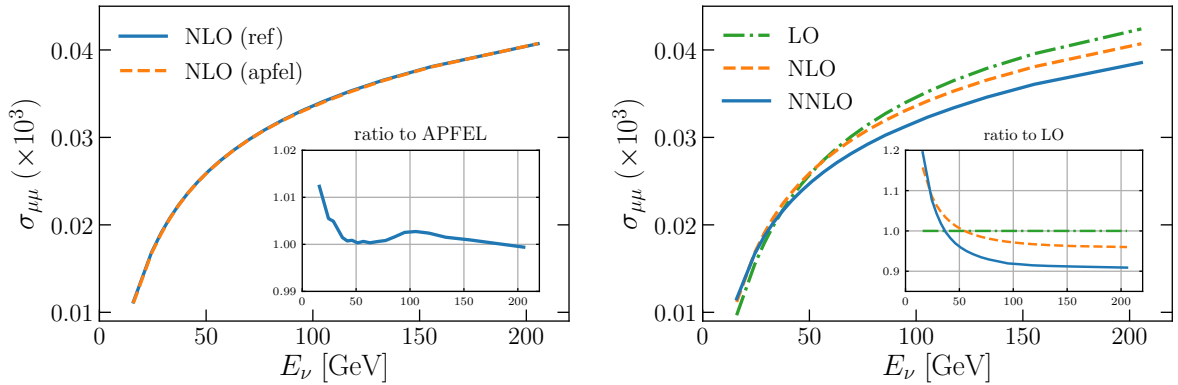


Figure 2.1. Left: the integrated dimuon cross section as a function of the neutrino beam energy E_ν , Eq. (2.1) (with $i = \mu\mu$), computed at NLO in the kinematic range measured by the NOMAD experiment with APFEL (apfel) and with a code based on [33] (ref). The ratio of the two computations is shown in the inset. Right: the same cross section computed in the FFN scheme ($n_f = 3$) with the NNPDF3.1 NNLO PDF set (also the $n_f = 3$ version) for various perturbative orders. The inset displays the ratio to the LO calculation.

the inclusive ($i = \text{CC}$, entering the denominator of $\mathcal{R}_{\mu\mu}$) charged-current cross section

$$\frac{d^2\sigma_i}{dx dQ^2}(x, Q^2, E_\nu) = \frac{G_F^2 M_W^2}{4\pi} \frac{1}{(Q^2 + M_W^2)^2} \times \left[\left(Y_+ - \frac{2m_p^2 x^2 y^2}{Q^2} \right) F_2^i(x, Q^2) - y^2 F_L^i(x, Q^2) + Y_- x F_3^i \right] K^i. \quad (2.2)$$

The kinematic factors $Y_\pm = 1 \pm (1 - y)^2$ are related to the inelasticity $y = Q^2/(2m_p E_\nu x)$; G_F and M_W are respectively the Fermi constant and the mass of the W boson. The factor K^i is either the identity, for $i = \text{CC}$, or the charm semileptonic branching ratio B_μ , for $i = \mu\mu$. In the latter case we use the E_ν -dependent parametrization $B_\mu(E_\nu) = a(1 + b/E_\nu)^{-1}$, with the values of the parameters a and b determined in [10], $a = 0.097 \pm 0.003$ and $b = 6.7 \pm 1.8$. The corresponding uncertainty is included in the experimental covariance matrix of the measurement.

Both the charm (for $i = \mu\mu$) and the total (for $i = \text{CC}$) structure functions F_p^i ($p = 2, L, 3$) entering Eq. (2.2) are evaluated with APFEL [32]. We benchmarked our results against those obtained from an independent computation based on [33]. After the correction of a bug in APFEL, which affected the computation of the large- x DIS coefficient functions at next-to-leading (NLO) order, the relative difference between the two is found to be of the order of permille, apart from the lowest E_ν bins, in which it reaches the percent level, as displayed in the left panel of Fig. 2.1.

2.2.2 Theoretical improvements

In comparison to the earlier NNPDF analyses [19,27], here we introduce several theoretical improvements, which are summarized in turn below.

NNLO massive corrections in neutrino DIS. We incorporate the recently computed NNLO charm-quark massive corrections [33,34] in the description of the NuTeV and NOMAD measurements. We do so by multiplying the NLO theoretical prediction in the FONLL general-mass variable flavor number scheme [35,36] by a K -factor defined as the ratio between the NNLO result in the fixed-flavor number (FFN) scheme with and without the charm-mass correction in the matrix elements (ME); NNLO PDFs are used

in both cases. The resulting K -factor

$$K_{\text{NNLO}} \equiv \frac{\sigma_{\text{FFN}}(\text{NNLO PDFs, NNLO ME})}{\sigma_{\text{FFN}}(\text{NNLO PDFs, NLO ME})}, \quad (2.3)$$

is such that the prediction for the NuTeV dimuon cross sections becomes

$$\left. \frac{d^2\sigma_{\mu\mu}}{dx dQ^2} \right|_{\text{FONLL (NNLO ME)}} = K_{\text{NNLO}} \times \left. \frac{d^2\sigma_{\mu\mu}}{dx dQ^2} \right|_{\text{FONLL (NLO ME)}}, \quad (2.4)$$

and an analogous expression holds for the NOMAD observables.

This approach provides a good approximation of the exact result, because theoretical predictions in the FFN and FONLL schemes are very close for the NuTeV and NOMAD kinematics. This fact was demonstrated in [36] in the case of NuTeV data; we nevertheless checked that it remains true with the independent computation of [33, 34], and that it also applies to the NOMAD measurements. To this purpose, we computed the relative difference between the FONLL-A and FFN scheme predictions for the NuTeV and NOMAD datasets based on structure functions accurate to $\mathcal{O}(\alpha_s)$. We found that differences were less than 1% in the entire kinematic range for NuTeV, and of about 1.5% irrespective of the value of E_ν for NOMAD. These differences are well below the experimental and the PDF uncertainties.¹ We therefore conclude that using a NNLO K -factor determined in the FFN scheme in fits that otherwise use the FONLL scheme throughout is unlikely to affect the final results. Given the current implementation of the FONLL scheme in the DIS observables [35] the matching between the NNLO massless and massive calculations would require non-trivial modifications of the code of [33], *e.g.* to extract the collinear logarithms, with little practical advantage.

The K -factors are in general smaller than unity, and thus enhance the (anti-)strange quark PDF when accounted for in the fit. This fact is consistent with what was already observed in [21], and is further illustrated in the right panel of Fig. 2.1, where we display the charm production cross section, Eq. (2.1), with $i = \mu\mu$, as a function of E_ν in the kinematic range measured by the NOMAD experiment. The cross section is obtained in the FFN scheme (with $n_f = 3$) at different perturbative orders using the NNPDF3.1 NNLO PDF set (consistently with $n_f = 3$). The inset displays the ratio to the leading order (LO) calculation. Higher-order corrections clearly suppress the cross section, in particular as E_ν increases. For instance, in the highest energy bin the NNLO cross section is about 10% smaller than the LO one. The size of the NNLO correction is comparable to or larger than the size of the NLO one, therefore its inclusion is mandatory to achieve a good description of the data. While the comparison of Fig. 2.1 is presented in the FFN scheme, all the fits discussed below are based on the FONLL scheme.

NNLO corrections in collider gauge boson production. Theoretical predictions for inclusive W - and Z -boson production and for W -boson production in association with charm quarks or light jets are evaluated at NLO using MCFM+APPLGRID [37, 38], and are supplemented with NNLO QCD K -factors. These are evaluated with FEWZ [39] for inclusive gauge boson production, and with the N_{jettty} program [40, 41] for W -boson production with light jets. In the first case, a fixed factorization and renormalization scale is used, equal to the mass of the gauge boson; in the second case, a dynamic scale is used, where the factorization and renormalization scales are defined as $\mu_F = \mu_R = \sqrt{m_W^2 + p_{T,j}^2}$, with m_W the mass of the W boson and $p_{T,j}$ the transverse momentum of the hadronic jet. Because NNLO QCD corrections for $W+c$ production have been presented only very recently [42], in this case we accompany the data with an additional correlated uncertainty, estimated from the 9-point scale variations of the NLO calculation [43, 44].

¹A $\simeq 1.5\%$ difference in K_{NNLO} corresponds to at most a $\simeq 0.1\%$ effect in the absolute cross sections.

Nuclear corrections in neutrino DIS. Neutrino-DIS measurements from the NuTeV and NOMAD experiments are subject to nuclear corrections, because they both utilize an iron (Fe) target. In this analysis, however, we do not include such corrections because they are expected to be subdominant in comparison to other sources of uncertainties. For NuTeV, they were found to be moderate in a global fit based on the same methodology used here [45]; for NOMAD, they are known to approximately cancel out in the ratio $\mathcal{R}_{\mu\mu}$. To verify this last statement, we recomputed the NOMAD ratio $\mathcal{R}_{\mu\mu}$ with the recently presented nNNPDF2.0 NLO Fe nuclear PDF set [46], and compared the result with the predictions obtained with the NLO free proton PDF set consistently determined in [46]. The full set of correlations between Fe and proton PDFs were therefore appropriately taken into account. The relative difference between the two computations (with and without nuclear PDF corrections) turned out to range between 3%, in the lowest E_ν bin, and a fraction of percent, in the bins at the highest E_ν . These differences are smaller than both the data and PDF uncertainties, therefore ignoring nuclear PDF uncertainties is a well-justified approximation. We note that nuclear non-isoscalarity effects are treated as in [45]. In the future, it might be interesting to extend the present analysis in a way that systematically accounts for nuclear PDF uncertainties.

Positivity of cross sections. We enforce the positivity of the charm structure function F_2^c with a procedure similar to that described in [47] for light quarks. This additional positivity constraint is required to prevent the fitted charm PDF becoming unphysically negative once the new datasets are included in the fit.

2.3 PDF sets

We assess the impact of the datasets and of the theoretical choices outlined in Sects. 2.1-2.2 on PDFs by performing the series of fits summarized in Table 2.1. All of them are accurate to NNLO in perturbative QCD (where available), and are based on the NNPDF methodology, see [47] and references therein for a comprehensive description.

The first fit (`str_base`) is our baseline, and corresponds to the fit of [27] with the addition of the NNLO charm-mass K -factors for the NuTeV data and of the positivity constraint on F_2^c , and with the removal of the 2010 and 2011 ATLAS W, Z inclusive measurements of [11, 12]. We will present a comparison of this baseline fit with the NNPDF3.1 PDF set of [19] in Sect. 3.3. This fit is then supplemented with all the new LHC data, including the ATLAS W, Z measurements from [11, 12], to obtain the second fit (`str_prior`), for which we generate $N_{\text{rep}} = 850$ Monte Carlo replicas. The exclusion of the ATLAS W, Z measurements of [11, 12] from the `str_base` fit allows us to quantify the effect of the full LHC strangeness-sensitive dataset by comparing this fit with the `str_prior` one. This second fit, `str_prior`, is finally further supplemented with the NOMAD data, specifically the set that depends on E_ν , to determine the third fit (`str`). Bayesian reweighting and unweighting [48, 49] are used in this last step, because they allow one to evaluate the two-dimensional integral in Eq. (2.1) only once, a task that would otherwise be computationally very intensive in a fit. After reweighting, one ends up with $N_{\text{eff}} = 105$ effective replicas, from which we construct a set of $N_{\text{rep}} = 100$ replicas.

We also produced variants of these three fits. First of all, in order to assess the impact of the choice of the specific NOMAD dataset, we performed the `str_s_hat` fit, which is equivalent to the `str` fit, except for the fact that the NOMAD E_ν -dependent dataset is replaced by its $\sqrt{\hat{s}}$ -dependent counterpart. In this case, after reweighting one ends up with $N_{\text{eff}} = 135$ effective replicas (out of $N_{\text{rep}} = 850$ initial replicas), from which we construct an ensemble of $N_{\text{rep}} = 100$ replicas. Second, in order to assess the impact of parametrizing the charm PDF, we performed the `str_prior_pch` and `str_pch` fits. These fits are equivalent to the `str_prior` and `str` fits, except for the fact that the charm PDF

Fit ID	Dataset	Theory
str_base	same as [27] – ATLAS W, Z [11, 12]	same as [27] + NNLO K -fact NuTeV F_2^c positivity
str_prior	same as str_base + ATLAS W, Z (full) [11, 12] ATLAS $W+c$ [16] CMS $W+c$ [17, 18] ATLAS W +jets [15]	same as str_base + correlated theory uncertainty for unknown NNLO QCD corrections
str	same as str_prior + NOMAD E_ν set [10]	same as str_prior + NNLO K -fact NOMAD
str_s_hat	same as str_prior + NOMAD \sqrt{s} set [10]	same as str
str_prior_pch	same as str_prior	same as str_prior , perturbative charm
str_pch	same as str_prior_pch + NOMAD E_ν set [10]	same as str_prior_pch + NNLO K -fact NOMAD

Table 2.1. A list of the PDF fits presented in this work, see text for details.

is generated perturbatively off the gluon and the light quark PDFs. In this case, we produced only $N_{\text{rep}} = 500$ replicas in the **str_prior_pch** fit; after reweighting we are left with $N_{\text{eff}} = 157$ effective replicas, from which we constructed an ensemble of $N_{\text{rep}} = 100$ replicas for the **str_pch** fit.

3 Results

In this section we present the main results of our analysis. First, we discuss the quality of the fits that we performed; then, we compare the data to our theoretical predictions; next, we present the PDFs that we determine; and finally, we revisit the strangeness content of the proton in light of them. We conclude by focusing on the impact of the NOMAD dataset and of the implications that the treatment of the charm PDF has on our results.

3.1 Fit quality

In Table 3.1 we summarize the values of the χ^2 per data point obtained from five of the six fits discussed in Sect. 2.3, see also Table 2.1: χ_{base}^2 for **str_base**; χ_{pr}^2 for **str_prior**; χ_{str}^2 for **str**; $\chi_{\text{str_s_hat}}^2$ for **str_s_hat**; and $\chi_{\text{str_pch}}^2$ for **str_pch**. The χ^2 of the **str_prior_pch** fit is not reported because it is not particularly more informative than the one of the **str_pch** fit, which includes the complete dataset. In all cases, the value of the χ^2 per data point correspond to the definition given in Eqs. (3.2)-(3.3) in [50]. The values in square brackets are for datasets not included in the corresponding fit.

We first assess the general consistency of the new experimental data, by comparing the values of the χ^2 of the first three fits. The description of the new datasets — which, in particular, is not optimal for the ATLAS W, Z dataset in the **str_base** fit and for the NOMAD dataset in the **str_base** and **str_prior** fits — markedly improves as soon as they are included in subsequent fits. The largest effect is witnessed by the NOMAD dataset, whose χ^2 per data point decreases from about 9 in the **str_base** and **str_prior** fits to about 0.6 in the **str** fit. The χ^2 for all of the other datasets is in general not affected upon the addition of the NOMAD dataset in the **str** fit, except for the NuTeV dataset, whose χ^2 is further improved in comparison to the **str_prior** fit. We therefore conclude that the global dataset is overall consistent and satisfactorily described in the

Process	Dataset	n_{dat}	χ_{base}^2	χ_{pr}^2	χ_{str}^2	$\chi_{\text{str_s_hat}}^2$	$\chi_{\text{str_pch}}^2$
$\nu\text{DIS } (\mu\mu)$		76/76/95/91/95	0.70	0.71	0.53	0.52	0.63
	NuTeV [9]	76/76/76/76/76	0.70	0.71	0.53	0.55	0.61
	NOMAD [10]	—/—/19/15/19	[9.0]	[8.8]	0.55	0.35	0.69
W, Z (incl.)		327/418/418/418/418	1.38	1.40	1.40	1.39	1.40
	ATLAS [12]	—/61/61/61/61	3.22	1.65	1.67	1.64	1.80
$W+c$		—/37/37/37/37	[0.76]	0.68	0.60	0.66	0.68
	CMS [17, 18]	—/15/15/15/15	[1.10]	0.98	0.96	1.00	1.00
	ATLAS [16]	—/22/22/22/22	[0.53]	0.48	0.42	0.43	0.46
$W+\text{jets}$	ATLAS [15]	—/32/32/32/32	[1.58]	1.18	1.18	1.18	1.18
Total		3917/4077/4096/4092/4096	1.17	1.17	1.17	1.17	1.20

Table 3.1. Values of the χ^2 per data point for the strangeness-sensitive datasets discussed in this work obtained from the `str_base`, `str_prior`, `str`, `str_s_hat`, and `str_pch` fits, see Table 2.1. Values in square brackets are for datasets not included in the corresponding fit.

final `str` fit.

We then assess the consistency of alternative NOMAD datasets by comparing the χ^2 of the `str` and `str_s_hat` fits. We recall that they include, respectively, the E_ν -dependent and the $\sqrt{\hat{s}}$ -dependent distributions. A very similar fit quality is achieved in the two cases, not only for the NOMAD dataset, but also for all of the other datasets: the differences in the values of the χ^2 between the two fits are smaller than statistical fluctuations. This fact suggests that the alternative NOMAD datasets are consistent between them and with the rest of the dataset. This conclusion is in line with the observation that a similar number of effective replicas is obtained by reweighting the `str_prior` fit with either dataset, see the discussion in Sect. 2.3.

We finally assess the effect of parametrizing the charm PDF (or not) by comparing the χ^2 of the `str` and `str_pch` fits. We recall that the two fits contain exactly the same datasets, however in the former the charm PDF is parametrized on the same footing as the other light quark PDFs, while in the latter it is generated perturbatively off the light quarks and the gluon. The fitted charm fit (`str`) achieves a better description of the strangeness-sensitive datasets, and of the global dataset overall, than the perturbative charm fit (`str_pch`). We note in particular the χ^2 values of the ATLAS W, Z and of the total datasets, which increase respectively from 1.67 to 1.80 and from 1.17 to 1.20 when comparing the `str` and the `str_pch` fits. We therefore confirm previous studies indicating that fitting the charm PDFs improves the description of the experimental data within a global PDF analysis.

3.2 Comparison with experimental data

We now compare the strangeness-sensitive datasets included in our analysis with the corresponding theoretical predictions. Our aim is to assess the impact of the various datasets. To this purpose, we compare the fits obtained without and with a specific dataset included.

We first focus on the neutrino-DIS datasets. In Fig. 3.1 we display the comparison for the E_ν -dependent and the $\sqrt{\hat{s}}$ -dependent NOMAD measurements. We compare the theoretical predictions obtained from the `str_prior` fit and, respectively, either from the `str` or the `str_s_hat` fits. The insets display the ratio to the central value of each measured data point. In the two cases, we observe a consistent picture: the theoretical prediction obtained from the `str_prior` fit overshoots the data points by about 20% (10%) for the E_ν -dependent ($\sqrt{\hat{s}}$ -dependent) dataset; after reweighting, the theoretical prediction nicely describes the data points with an uncertainty consistently reduced by up to a factor

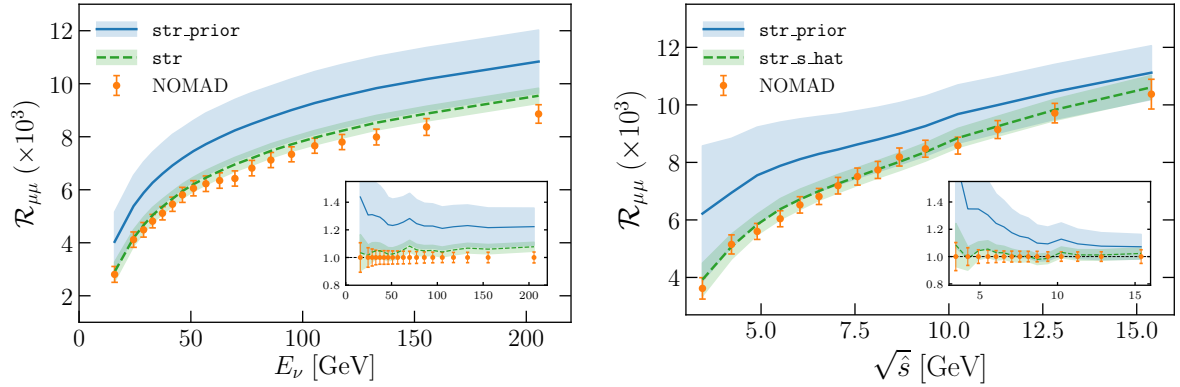


Figure 3.1. Comparison between the theoretical predictions, obtained from the `str_prior` and `str` (left) or `str_s_hat` (right) fits, and the experimental data for the E_ν - and $\sqrt{\hat{s}}$ -dependent NOMAD measurements. The insets display the ratio to the central value of each data point. The error bands on the theory predictions indicate the one-sigma PDF uncertainties.

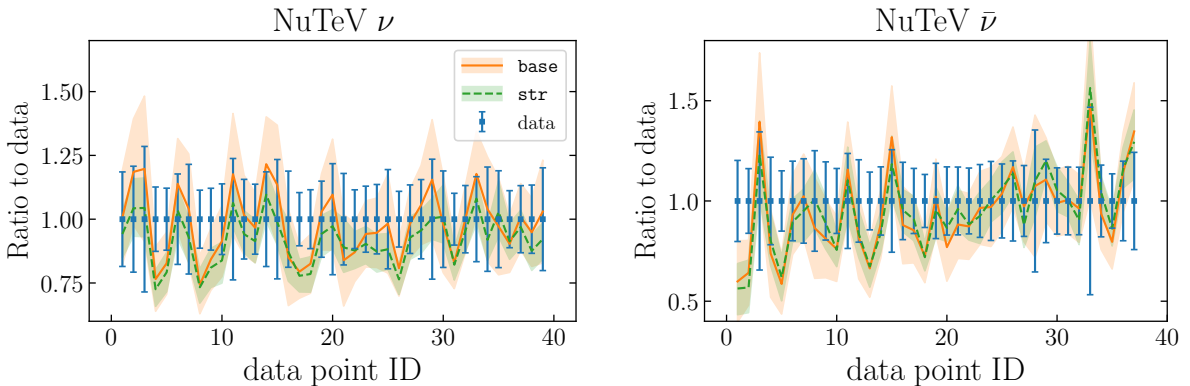


Figure 3.2. Comparison between theoretical predictions and experimental data for the neutrino (left) and antineutrino (right) charm dimuon cross sections measured by the NuTeV experiment [9]. Data and theory are normalized to the central value of the former; data points are sorted by their ID values, roughly corresponding to increasing x and Q^2 values (for fixed pseudo-rapidity bins y) when the plots are read from left to right.

of four. We explicitly checked that the same reduction of the uncertainty occurs also in the case of perturbative charm fits without (`str_prior_pch`) and with (`str_pch`) the E_ν -dependent NOMAD dataset included. In this case, however, the underlying PDFs and the strangeness ratio R_s vary in comparison to fitted charm fits, as discussed in Sect. 3.4.

In Fig. 3.2 we display the data/theory comparison for the charm dimuon cross sections from the NuTeV measurement of [9] (for both neutrino and antineutrino beams). In this case, predictions are determined from the `str_base` and `str` PDF input sets, and are normalized to the central value of the data points. These are sorted by their ID value, roughly corresponding to increasing x and Q^2 values (for fixed pseudo-rapidity bins y) when the plot is read from left to right. A fair agreement between data and theory is observed, as expected from the pattern of the χ^2 values reported in Table 3.1. The inclusion of the NOMAD data in the `str` fit suppresses the theoretical expectation for the NuTeV neutrino cross sections (but not for the antineutrino ones, for which no analogue observable is measured by NOMAD); uncertainties are reduced by up to a factor of two (again, more markedly for the neutrino data points than for the antineutrino ones). Both the shift in the central value and the reduction of the uncertainty remain smaller than the comparatively large experimental uncertainty.

We now turn to the hadron collider data. In Fig. 3.3 we display: the $W+c$ lepton rapidity distributions corresponding to the ATLAS measurement of [16] (for both W^+ and

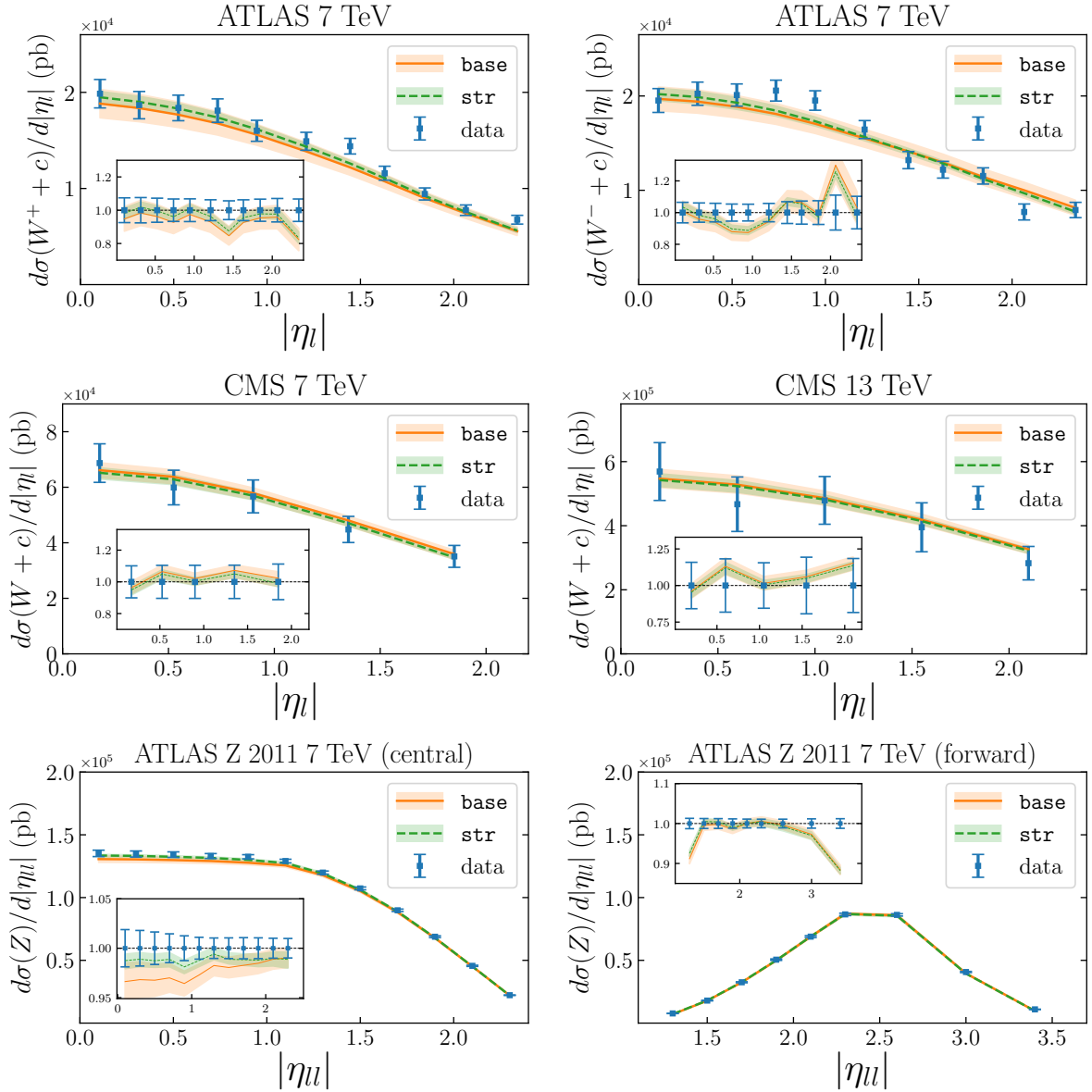


Figure 3.3. Comparison between theoretical predictions and experimental data for some of strangeness-sensitive proton collider measurements used in this work. Top: the $W+c$ lepton rapidity distributions (separately for W^+ and W^-) corresponding to the ATLAS measurement at 7 TeV [16]. Middle: the $W+c$ lepton rapidity distributions (sum of W^+ and W^-) corresponding to the CMS measurements at 7 TeV [17] and 13 TeV [18]. Bottom: the Z dilepton rapidity distributions from the ATLAS measurement of [12]. The insets display the theory to data ratio. Theoretical predictions are evaluated with the `str_base` and `str` fits.

W^-) and to the CMS measurements (sum of W^+ and W^-) of [17, 18] (respectively at a c.m.e. of 7 TeV and 13 TeV); and the Z dilepton rapidity distributions from the ATLAS measurement of [12] at a c.m.e. of 7 TeV (for both the central and forward selection cuts). The insets display the ratio of the theory to the central value of the experimental measurement. As in Fig. 3.2, theoretical predictions are evaluated with the `str_base` and `str` PDF sets.

A fair agreement between data and theory is found in all cases, as expected from the pattern of χ^2 values reported in Table 3.1. However, we clearly see that the size of the PDF uncertainty relative to the size of the data uncertainty depend on the dataset. Concerning the ATLAS and CMS $W+c$ measurements, experimental uncertainties span the range between 10% and 20%, and are consistently larger than PDF uncertainties. We note that the PDF uncertainties in the theory predictions are markedly reduced

in the `str` fit in comparison to `str_base` fit, as highlighted by the ratios in the insets. Concerning the ATLAS Z distribution, the total experimental uncertainty is much smaller than the W counterpart, around 2% for the central rapidity bin, and in the central region it is comparable to the PDF uncertainty. We therefore expect this measurement to be one of the most constraining amongst all of the LHC measurements considered in this work. Interestingly, once the NOMAD dataset is included in the fit, the central value of the theoretical prediction approaches the central value of the ATLAS data, and PDF uncertainties are slightly reduced. A similar trend can be observed for the forward selection data. This behaviour is a further sign of the good overall compatibility of all of the datasets, and in particular of neutrino DIS and LHC gauge boson production measurements.

3.3 Parton distributions

We now turn to study the impact of the theoretical assumptions and of the new datasets considered in this analysis on the PDFs. We first present a comparison between the `str_base` and the NNPDF3.1 parton sets, and then a comparison amongst the `str_base`, `str_prior` and `str` PDF sets. In the latter case, because the new datasets are expected to mainly affect the strange quark and anti-quark distributions, we will focus on the total and valence strange distributions, first, and on the other PDFs, then.

3.3.1 Comparison with NNPDF3.1

Our baseline fit `str_base` differs from NNPDF3.1 [19] in several respects. As explained in Sect. 2.2, these include: the treatment of inclusive jet production from ATLAS and CMS with NNLO K -factors, see [27]; an updated treatment of non-isoscalarity effects in neutrino-DIS data, see [45]; the inclusion of the NNLO massive corrections to the NuTeV structure functions; the new F_2^c positivity constraint; and the correction of the APFEL bug found in the benchmark reported in Fig. 2.1, which affected the large- x implementation of the NLO coefficient functions. Furthermore following the motivation presented in Sect. 2.3, the ATLAS W, Z rapidity distributions from [11, 12] that were part of NNPDF3.1 are excluded from `str_base`.

In order to gauge the impact of all these differences, in Fig. 3.4 we compare the NNPDF3.1 and `str_base` parton sets. We display the up (valence and sea), down (valence and sea), strange (valence and total), gluon, and charm distributions at a scale $Q = 100$ GeV; PDFs are normalized to the central value of the NNPDF3.1 parton set, except for the strange valence distribution, for which the absolute PDFs are shown. In addition, we also display in this comparison the results of a variant of `str_base` obtained without the NNLO K -factors, Eq. (2.3), for the NuTeV cross sections, in order to isolate their impact in the resulting PDFs.

In comparison to NNPDF3.1, in the `str_base` fit we observe: a rearrangement of the quark flavor separation at medium and large x ; an increase in the central value of the strange PDF for $x \gtrsim 10^{-3}$; a similar effect in the case of the charm PDF for $x \gtrsim 10^{-2}$ (mostly due to the new F_2^c positivity constraint); and a harder gluon at large x (mostly due to the improved NNLO treatment of jet data). All in all, while the two fits agree within uncertainties, the improvements introduced in the `str_base` fit lead to PDF differences that are sufficiently large to adopt it as baseline in the current study. Therefore the NNPDF3.1 set will not be discussed further in the sequel.

From the comparison of `str_base` with its variant without the K -factors, the most noticeable effect is the moderate suppression of s^+ in the region $x \gtrsim 0.05$, which can represent a shift of up to half a sigma in units of the PDF uncertainty. One can also observe a small correlated enhancement of the up and down quark sea distributions in the

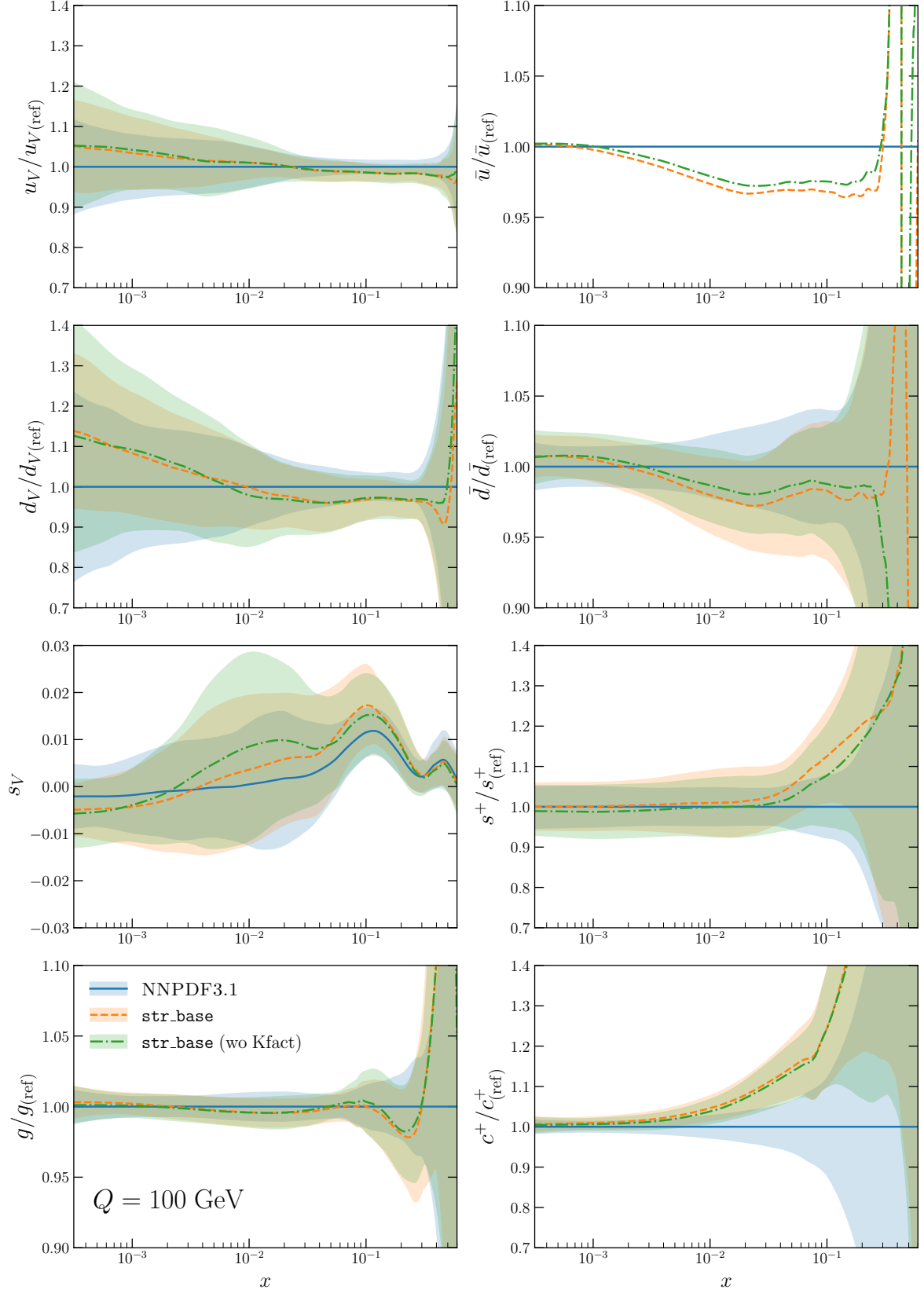


Figure 3.4. Comparison between the NNPDF3.1 NNLO fit [19] and the baseline fit used in this work, `str_base`. From top to bottom and left to right we show the up (valence and sea), down (valence and sea), strange (valence and total), gluon, and charm distributions at a scale $Q = 100$ GeV; PDFs are normalized to the central value of the NNPDF3.1 parton set (ref), except for the strange valence distribution, for which the absolute PDFs are shown.

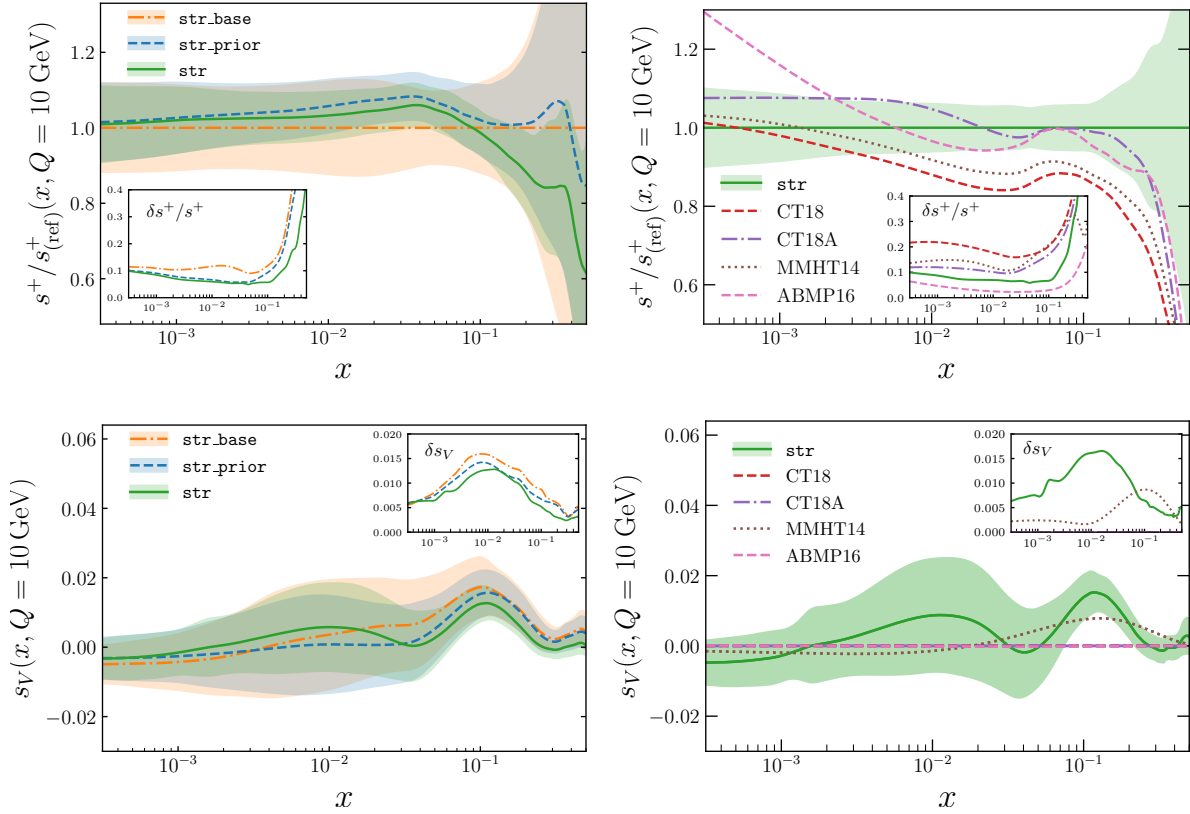


Figure 3.5. A comparison of the total (top) and valence (bottom) strange distributions, s^+ and s_V , at $Q = 10$ GeV. PDFs are from the `str_base`, `str_prior` and `str` fits (left panels) and from the `str` and other recent PDF fits (right panels), see text for details. The total strangeness s^+ is normalized to the central value of the `str_base` fit. The insets display the corresponding relative ($\delta s^+ / s^+$) and absolute (δs_V) PDF uncertainties.

same region of x . The impact of the K -factors turns out to be negligible for the gluon and other flavour combinations.

3.3.2 Total and valence strange distributions

In Fig. 3.5 we display the total and valence strange distributions at $Q = 10$ GeV. We compare in turn the PDFs obtained from the `str_base`, `str_prior` and `str` fits, and those obtained from the `str` fit with other recent parton sets. Specifically, we consider CT18, CT18A [20] (CT18A is a variant of CT18 that includes the ATLAS W , Z data), MMHT14 [51], and ABMP16 [52]. They all include only a subset of the strangeness-sensitive data included in our analysis (see Table 3.1), in particular: the NuTeV dataset is part of all PDF sets; the NOMAD dataset is only part of ABMP16; and the off-peak and forward ATLAS W , Z bins, the $W+c$ and the W +jets datasets are not part of any of these PDF sets. We also emphasize that, apart from the more extensive dataset, our analysis differs from all of the other PDF determinations shown in Fig. 3.5 in that the charm-quark PDF is fitted on the same footing as the other light-quark PDFs [53]. This feature was demonstrated to improve the description of DIS and LHC datasets, and in particular to partially relieve tensions between the NuTeV and the ATLAS W , Z datasets [19]. The insets in Fig. 3.5 display the relative and absolute PDF uncertainties for the total ($\delta s^+ / s^+$) and valence (δs_V) strange distributions, respectively. In the case of s^+ , the curves are normalized to the central value of the `str_base` fit.

A comparison amongst the `str_base`, `str_prior` and `str` fits reveals that the impact of the data is consistent for the total and valence strange distributions. The inclusion

of the LHC datasets in the `str_prior` fit does not alter the central value of the PDFs in a significant way, while it narrows the PDF uncertainty across most of the x range. The inclusion of the NOMAD dataset in the `str` fit is associated to a larger effect: the central value of both s^+ and s_V is suppressed by about 20% (or more) for $x \gtrsim 0.1$; the uncertainty is further reduced by up to a third in the same x region.

A comparison amongst the `str` fit and other recent parton sets reveals differences in the shape of the central value of the s^+ and s_V distributions. In the second case, in particular, only MMHT14 [51] allows for a non-zero parametrization. Within the larger uncertainties of the CT18, CT18A and MMHT14 PDF sets, however, results are overall consistent. In this respect, note that the very small uncertainty of the ABM16 set is an artifact of the lack of a tolerance criterion in their analysis. In this case, uncertainties should be rescaled by a factor which is however not determined in their analysis.

3.3.3 Light quark, charm, and gluon PDFs

In Fig. 3.6 we compare the up (valence and sea), down (valence and sea), gluon and charm distributions resulting from the `str_base`, `str_prior` and `str` fits at $Q = 100$ GeV. Results are normalized to the `str_base` fit.

From these comparisons, we observe that the new datasets have a little impact on the gluon PDF, both on central values and on uncertainties, as expected. A bigger effect is observed instead on the quark PDFs. For light quarks and antiquarks, the electroweak LHC datasets constrain the distributions at low to mid values of x , $x \lesssim 0.1$, while the NOMAD datasets do so at larger values of x , $x \gtrsim 0.1$. The two datasets are therefore complementary, and concur together to enhance the central value of the down distributions in the region $0.01 \lesssim x \sim 0.1$ by a few percent, and to make all the light valence and sea quark PDFs more precise: overall, uncertainties are reduced by up to a factor 2 in the same region for the `str` fit. For the charm PDF, the central value is suppressed in the `str` fit; uncertainties are reduced by up to a factor 2 for $x \simeq 0.05$. This effect is almost entirely due to the NOMAD data, which is indirectly sensitive to the charm PDF through its interplay with the $s\bar{c}$ and $\bar{s}c$ contributions to W -boson production.

3.4 The strange content of the proton revisited

We finally revisit the strange content of the proton in light of our results. To this purpose, we consider the strange fraction of proton quark sea and the corresponding ratio of momentum fraction, respectively defined as

$$R_s(x, Q^2) = \frac{s(x, Q^2) + \bar{s}(x, Q^2)}{\bar{u}(x, Q^2) + \bar{d}(x, Q^2)}, \quad K_s(Q^2) = \frac{\int_0^1 dx x [s(x, Q^2) + \bar{s}(x, Q^2)]}{\int_0^1 dx x [\bar{u}(x, Q^2) + \bar{d}(x, Q^2)]}. \quad (3.1)$$

We first consider the ratio R_s . In the left panel of Fig. 3.7 we display it for the `str_base`, `str_prior` and `str` fits at a scale $Q = 10$ GeV as a function of x . The inset displays the associated relative PDF uncertainty $\delta R_s/R_s$. The impact of the new datasets is clearly visible. Concerning the central value, collider datasets do not alter its expectation (the results obtained from the `str_base` and `str_prior` fits are almost identical); the NOMAD dataset, instead, prefers a more suppressed strange sea for $x \gtrsim 0.1$. Concerning uncertainties, collider datasets lead to a reduction of the relative uncertainty on R_s of about 4% for $x \lesssim 0.1$; the NOMAD dataset, instead, reduces it by about a factor of two for $x \gtrsim 0.1$. Overall, the impact of the new datasets depends on x , and is mostly significant for $x = 0.2$, where the uncertainty on R_s is reduced from 20% to 8%. For $x \gtrsim 0.3$ no experimental constraints are available, hence the PDF uncertainty blows up.

The right panel of Fig. 3.7 compares the ratio R_s , computed at a scale $Q = 10$ GeV as a function of x , as obtained from the `str` fit and from the CT18/CT18A [20], MMHT14 [51],

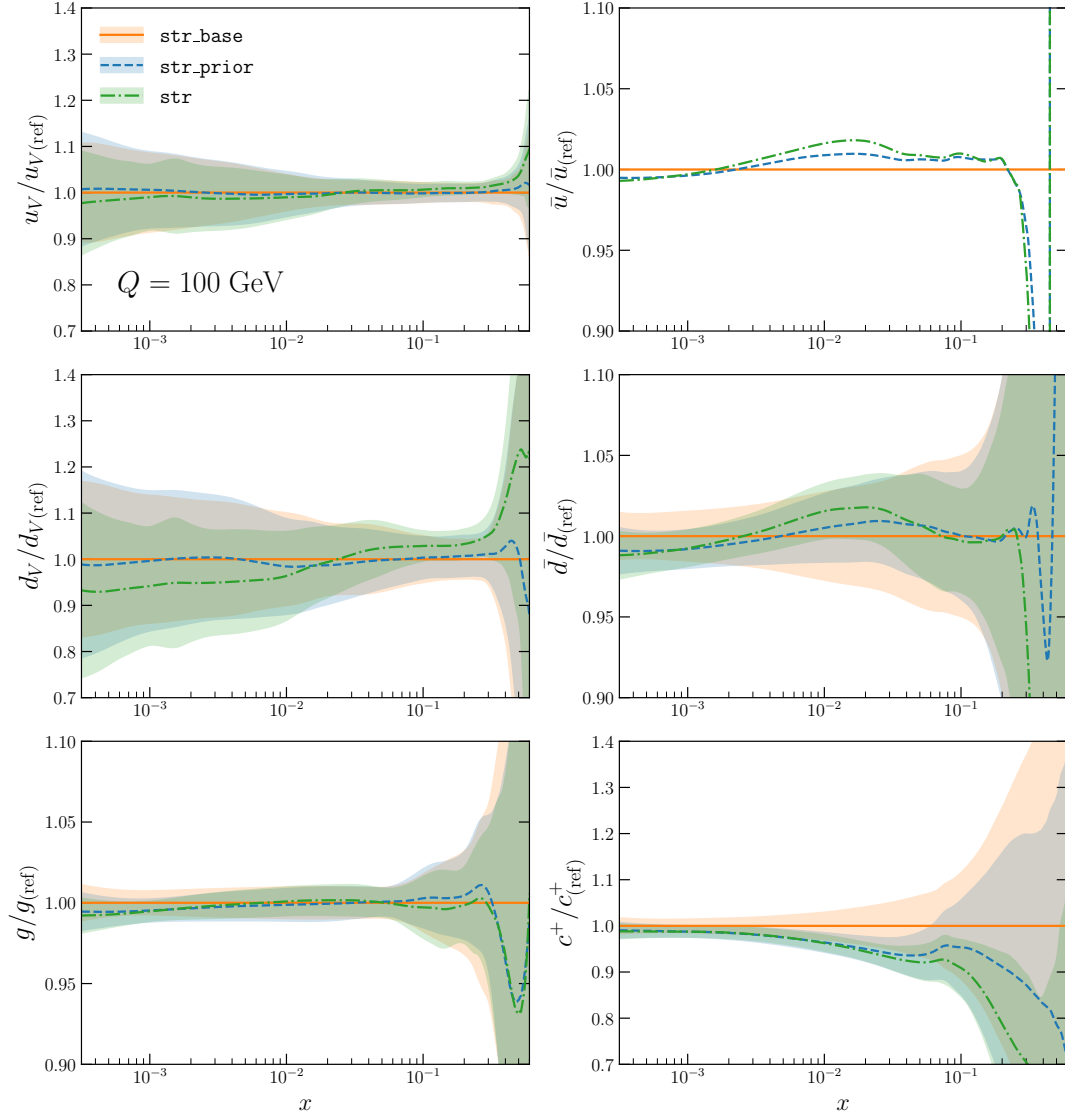


Figure 3.6. Comparison between the fits presented in this work. From top to bottom and left to right we show the up (valence and sea), down (valence and sea), gluon and charm distributions resulting from the `str_base`, `str_prior` and `str` fits at $Q = 100$ GeV. Results are normalized to the `str_base` fit (ref).

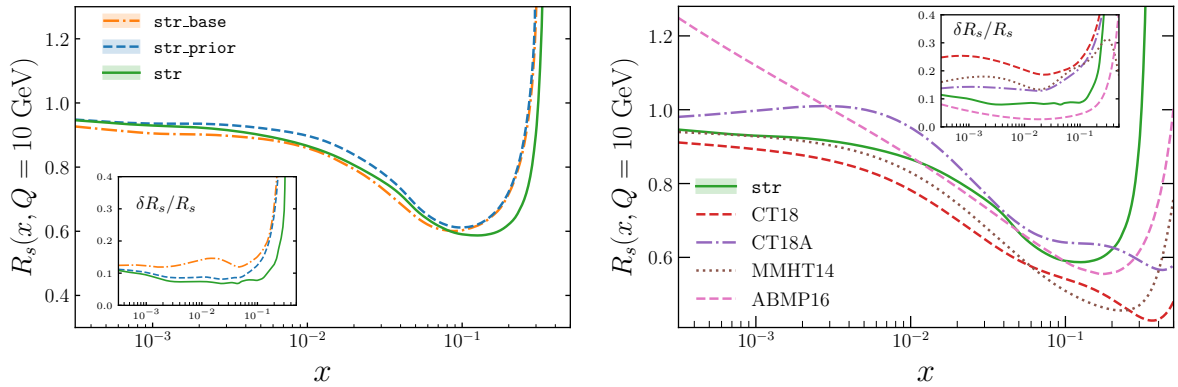


Figure 3.7. The ratio R_s , Eq. (3.1), as a function of x at $Q = 10$ GeV. The PDF used are from the `str_base`, `str_prior` and `str` fits (left), and from the `str` fit and from recent parton sets (right) see text for details. The insets display the corresponding relative uncertainty $\delta R_s/R_s$.

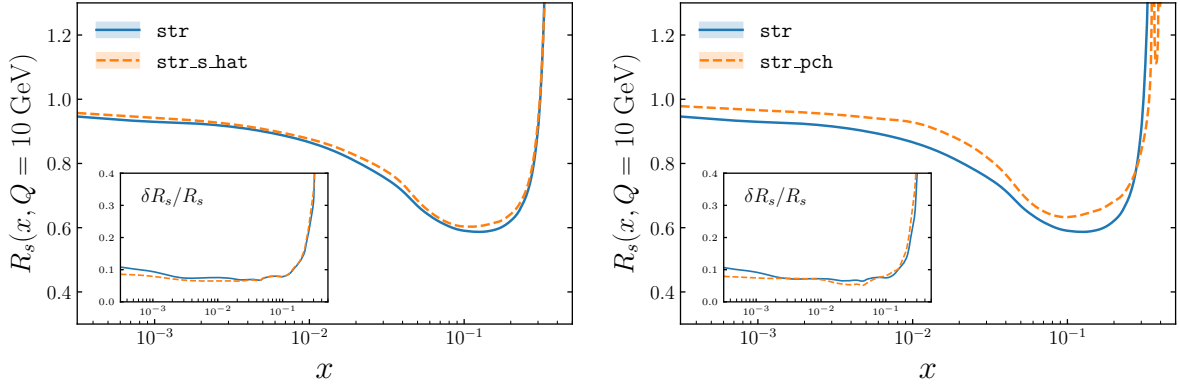


Figure 3.8. Same as Fig. 3.7, comparing fits to the E_ν -dependent (**str**) or to the $\sqrt{\hat{s}}$ -dependent (**str_s_hat**) NOMAD dataset (left), and fits with fitted (**str**) or perturbative (**str_pch**) charm (right).

and ABMP16 [52] fits. The inset displays the relative PDF uncertainty $\delta R_s/R_s$. Our **str** determination agrees with the CT18A and ABMP16 results within uncertainties in the data region. However it overshoots the CT18 and MMHT14 results. Note that the very small PDF uncertainties of the ABMP16 result should be realistically rescaled by a tolerance factor $T = \chi^2 > 1$ [1], which is however not accounted for in their analysis. With this caveat, our results for s^+ and R_s are also the most precise, in particular around $x \sim 0.1$, thanks to the wider dataset (and specifically of NOMAD) employed to constrain the strange quark and anti-quark PDFs.

We explicitly assessed how the results for R_s obtained with our optimal fit **str** depend on the specific choice of the NOMAD dataset and on the fact that the charm PDF is parametrized on the same footing as light quark PDFs. In Fig. 3.8 we display the ratio R_s , as a function of x at $Q = 10$ GeV: in the left panel we compare results obtained with the **str** and **str_s_hat** fits; in the right panel, we compare results obtained with the **str** and **str_pch** fits. In the first case, both the central value and the PDF uncertainties of R_s are very similar. This fact confirms the independence of our results upon the choice of the NOMAD dataset included in the fit. In the second case, while PDF uncertainties turn out to be very similar in both the perturbative and in the fitted charm fits, the former prefers a central value which is systematically larger than the one obtained from the latter. The size of the shift, however, is at most as large as one-sigma in units of the PDF uncertainties, in line with previous studies [19].

In order to further investigate how our results compare to those reported in the ATLAS studies [11, 12], which claimed a symmetric strange quark sea, in Fig. 3.9 we display the values of R_s for the **base**, **prior** and **str** fits and for the fits shown in Fig. 3.7. Here R_s is evaluated for the two kinematic choices outlined in [11, 12], first $x = 0.023$ and $Q = 1.6$ GeV, and second for $x = 0.13$ and $Q = 100$ GeV. Fig. 3.9 makes it clear the consistent effect of the new datasets included in our analysis. Considering the results for R_s at $x = 0.023$ and $Q = 1.6$ GeV, the value of $R_s = 0.69 \pm 0.22$ in the **str_base** fit is made more precise by the LHC datasets, which reduce its uncertainty by about a factor two, while also increasing its central value, $R_s = 0.76 \pm 0.12$; then the neutrino-DIS NOMAD dataset shifts this number towards a lower value by a half-sigma bringing in also a further moderate reduction of the uncertainty, $R_s = 0.71 \pm 0.10$. We therefore conclude that the result $R_s = 1.13 \pm 0.11$, reported in [12] from an analysis of HERA and ATLAS W, Z data within the xFITTER framework [54], is not compatible with ours, possibly because it is affected by a restricted dataset and/or methodological limitations. Similar remarks also apply to the results for R_s at $x = 0.13$ and $Q = 100$ GeV, for which we observe a consistent slight reduction of the central value of R_s , and a larger reduction of

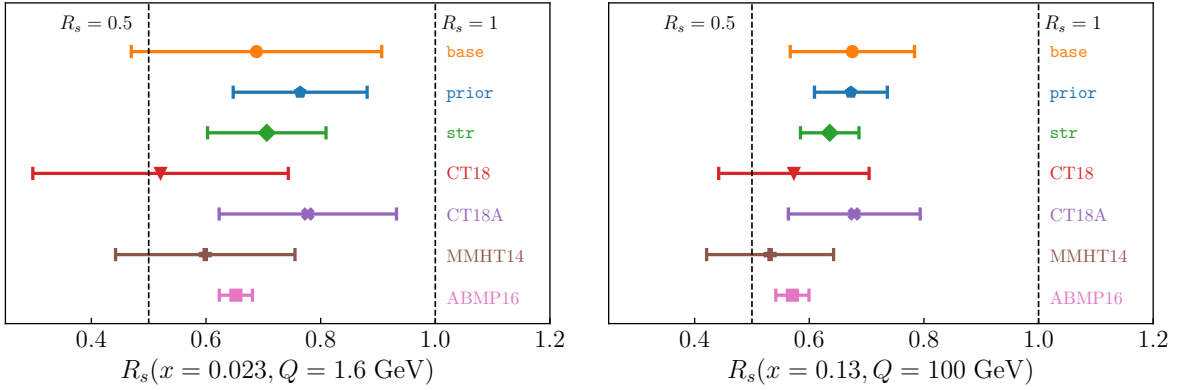


Figure 3.9. The ratio R_s , Eq. (3.1), computed at $x = 0.023$, $Q = 1.6$ GeV (left) and $x = 0.13$, $Q = 100$ GeV (right). The PDF sets are from the `str_base`, `str_prior`, `str` fits and from other recent PDF analyses, see the text for details.

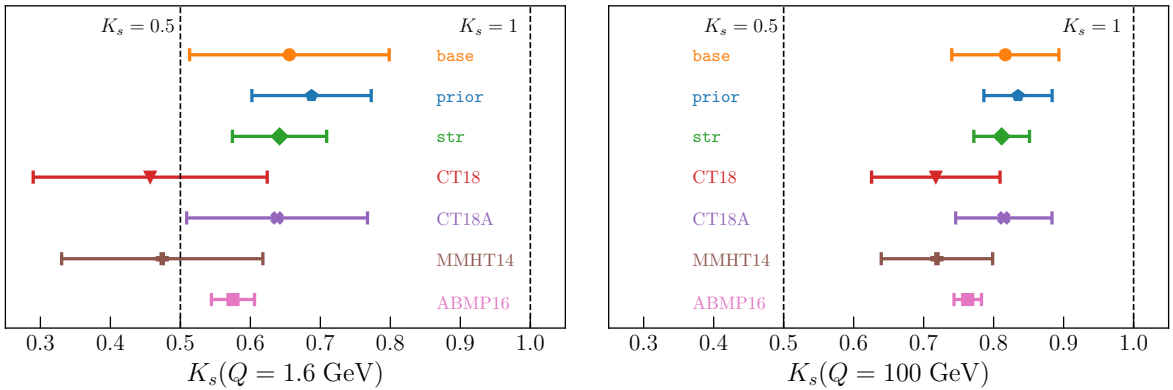


Figure 3.10. The ratio K_s , Eq. (3.1), for $Q = 1.6$ GeV (left) and $Q = 100$ GeV (right). The PDF sets are the same as in Fig. 3.9.

the uncertainty due to the stronger effect of NOMAD data at larger x , see Fig. 3.7. Our results are compatible, within uncertainties, with those of the other PDF determinations, but are generally more precise.

We finally consider the ratio of momentum fraction K_s , defined in Eq. (3.1). Fig. 3.10 displays K_s for $Q = 1.6$ GeV and $Q = 100$ GeV, respectively. The qualitative interpretation of this quantity is consistent with that of R_s , in particular, PDF uncertainties are reduced by a factor of two in the `str` fit with respect to the `str_base` fit. The values of K_s grow with the scale Q , as expected due to DGLAP evolution effects: for instance, using the `str` fit, one finds $K_s = 0.64 \pm 0.07$ at $Q = 1.6$ GeV, and $K_s = 0.81 \pm 0.04$ at $Q = 100$ GeV. Overall, our final `str` result indicates that the strange sea is mildly suppressed with respect to the rest of the light sea quarks. The value of K_s lies halfway a highly suppressed ($K_s \sim 0.5$) and a purely symmetric ($K_s = 1$) scenarios. As for R_s , our final `str` result for K_s is in agreement with the determinations obtained by other recent PDF analyses within uncertainties, although our results are generally more precise.

4 Summary

By means of a state-of-the-art global analysis, which combines all the relevant experimental and theoretical inputs, we have achieved a precise determination of the strangeness content of the proton. We have demonstrated the compatibility of a wide range of strangeness-sensitive datasets; quantified their relative impact on the fit; compared our

results to other recent global analyses; and assessed the robustness of our results with respect to various methodological choices. Our analysis demonstrates that the strange PDF can be precisely determined and that, after all, the proton is not too *strange*: the momentum fraction carried by strange quark and antiquark PDFs ranges between about 65% and 80% of the momentum fraction carried by the other light sea quarks in a wide energy range ($1.6 \text{ GeV} \leq Q \leq 100 \text{ GeV}$). The present determination of the strangeness content of the proton is found to agree, within uncertainties, with the results of other recent global PDF analyses.

Pivotal to this result is the complementary between the LHC gauge boson production data and of the charmed-tagged neutrino-DIS data, in particular from the NOMAD experiment. Our `str` PDF set, which combines all this information, is available in the LHAPDF format [55] together with its perturbative charm counterpart from

<http://nnpdf.mi.infn.it/nnpdf3-1strangeness/>

This analysis represents an important input for phenomenology, for instance to carry out improved determinations of fundamental parameters of the SM or to be used as baseline in the determination of nuclear PDFs, where strange distributions are not well known [46, 56, 57]. Our determination of the strange and anti-strange quark PDFs could be further stress-tested with more exclusive processes, *e.g.*, measurements of kaon production in semi-inclusive DIS (SIDIS). Studies of the strange PDFs based on SIDIS [58–60] notoriously prefer a suppressed strangeness, but are also subject to the potential bias coming from their sensitivity to the fragmentation of the strange quarks into kaons.

Acknowledgments

We are grateful to Jun Gao for providing us with the NNLO K -factors for the NuTeV and the NOMAD measurements, and for help into the benchmark of the corresponding NLO calculations. We thank Valerio Bertone for assistance with the usage of APFEL, Lucian Harland-Lang for discussions on the massive corrections to dimuon production, and Rabah Abdul-Khalek, Amanda Cooper-Sarkar, Stefano Forte, Katerina Lipka, Gavin Pownall and Cameron Voisey for comments on the manuscript. E.R.N. is supported by the European Commission through the Marie Skłodowska-Curie Action ParDHonS FFs.TMDs (grant number 752748). J.R. is partially supported by the Netherlands Organization for Scientific Research (NWO). M.U. and S.I. are partially supported by the STFC grant ST/L000385/1 and by the Royal Society grant RGF/EA/180148. The work of M.U. is also funded by the Royal Society grant DH150088 and supported by the European Research Council under the European Union’s Horizon 2020 research and innovation Programme (grant agreement n.950246).

References

- [1] J. Gao, L. Harland-Lang, and J. Rojo, *The Structure of the Proton in the LHC Precision Era*, Phys. Rept. **742** (2018) 1–121, [[arXiv:1709.04922](https://arxiv.org/abs/1709.04922)].
- [2] K. Kovarić, P. M. Nadolsky, and D. E. Soper, *Hadron structure in high-energy collisions*, Rev. Mod. Phys. **92** (2020), no. 4 045003, [[arXiv:1905.06957](https://arxiv.org/abs/1905.06957)].
- [3] J. J. Ethier and E. R. Nocera, *Parton Distributions in Nucleons and Nuclei*, Ann. Rev. Nucl. Part. Sci. (2020), no. 70 1–34, [[arXiv:2001.07722](https://arxiv.org/abs/2001.07722)].
- [4] **ATLAS** Collaboration, M. Aaboud et al., *Measurement of the W -boson mass in pp collisions at $\sqrt{s} = 7 \text{ TeV}$ with the ATLAS detector*, Eur. Phys. J. **C78** (2018), no. 2 110, [[arXiv:1701.07240](https://arxiv.org/abs/1701.07240)].

- [5] **CMS** Collaboration, A. M. Sirunyan et al., *Measurement of the weak mixing angle using the forward-backward asymmetry of Drell-Yan events in pp collisions at 8 TeV*, Eur. Phys. J. **C78** (2018), no. 9 701, [[arXiv:1806.00863](#)].
- [6] E. Bagnaschi and A. Vicini, *A new look at the estimation of the PDF uncertainties in the determination of electroweak parameters at hadron colliders*, [arXiv:1910.04726](#).
- [7] **CCFR** Collaboration, A. O. Bazarko et al., *Determination of the strange quark content of the nucleon from a next-to-leading order QCD analysis of neutrino charm production*, Z. Phys. **C65** (1995) 189–198, [[hep-ex/9406007](#)].
- [8] **CHORUS** Collaboration, A. Kayis-Topaksu et al., *Leading order analysis of neutrino induced dimuon events in the CHORUS experiment*, Nucl. Phys. B **798** (2008) 1–16, [[arXiv:0804.1869](#)].
- [9] D. Mason et al., *Measurement of the Nucleon Strange-Antistrange Asymmetry at Next-to-Leading Order in QCD from NuTeV Dimuon Data*, Phys. Rev. Lett. **99** (2007) 192001.
- [10] **NOMAD** Collaboration, O. Samoylov et al., *A Precision Measurement of Charm Dimuon Production in Neutrino Interactions from the NOMAD Experiment*, Nucl.Phys. **B876** (2013) 339, [[arXiv:1308.4750](#)].
- [11] **ATLAS** Collaboration, G. Aad et al., *Determination of the strange quark density of the proton from ATLAS measurements of the W, Z cross sections*, Phys.Rev.Lett. (2012) [[arXiv:1203.4051](#)].
- [12] **ATLAS** Collaboration, M. Aaboud et al., *Precision measurement and interpretation of inclusive W^+ , W^- and Z/γ^* production cross sections with the ATLAS detector*, Eur. Phys. J. **C77** (2017), no. 6 367, [[arXiv:1612.03016](#)].
- [13] **ATLAS** Collaboration, M. Sutton, *The PDF interpretation of the measurement of a vector boson produced in association with jets at the ATLAS detector*, PoS DIS2019 (2019) 034.
- [14] W. Stirling and E. Vryonidou, *Charm production in association with an electroweak gauge boson at the LHC*, Phys.Rev.Lett. **109** (2012) 082002, [[arXiv:1203.6781](#)].
- [15] **ATLAS** Collaboration, M. Aaboud et al., *Measurement of differential cross sections and W^+/W^- cross-section ratios for W boson production in association with jets at $\sqrt{s} = 8$ TeV with the ATLAS detector*, JHEP **05** (2018) 077, [[arXiv:1711.03296](#)].
- [16] **ATLAS** Collaboration, G. Aad et al., *Measurement of the production of a W boson in association with a charm quark in pp collisions at $\sqrt{s} = 7$ TeV with the ATLAS detector*, JHEP **1405** (2014) 068, [[arXiv:1402.6263](#)].
- [17] **CMS** Collaboration, S. Chatrchyan et al., *Measurement of associated W + charm production in pp collisions at $\sqrt{s} = 7$ TeV*, JHEP **02** (2014) 013, [[arXiv:1310.1138](#)].
- [18] **CMS** Collaboration, A. M. Sirunyan et al., *Measurement of associated production of a W boson and a charm quark in proton-proton collisions at $\sqrt{s} = 13$ TeV*, Eur. Phys. J. **C79** (2019), no. 3 269, [[arXiv:1811.10021](#)].

- [19] **NNPDF** Collaboration, R. D. Ball et al., *Parton distributions from high-precision collider data*, Eur. Phys. J. **C77** (2017), no. 10 663, [[arXiv:1706.00428](#)].
- [20] T.-J. Hou et al., *New CTEQ global analysis of quantum chromodynamics with high-precision data from the LHC*, [arXiv:1912.10053](#).
- [21] R. S. Thorne, S. Bailey, T. Cridge, L. A. Harland-Lang, A. Martin, and R. Nathvani, *Updates of PDFs using the MMHT framework*, PoS DIS2019 (2019) 036, [[arXiv:1907.08147](#)].
- [22] H. L. Lai et al., *The Strange Parton Distribution of the Nucleon: Global Analysis and Applications*, JHEP **04** (2007) 089, [[hep-ph/0702268](#)].
- [23] A. Kusina, T. Stavreva, S. Berge, F. Olness, I. Schienbein, K. Kovarik, T. Jezo, J. Yu, and K. Park, *Strange Quark PDFs and Implications for Drell-Yan Boson Production at the LHC*, Phys. Rev. D **85** (2012) 094028, [[arXiv:1203.1290](#)].
- [24] S. Alekhin, J. Blumlein, L. Caminadac, K. Lipka, K. Lohwasser, S. Moch, R. Petti, and R. Placakyte, *Determination of Strange Sea Quark Distributions from Fixed-target and Collider Data*, Phys. Rev. **D91** (2015), no. 9 094002, [[arXiv:1404.6469](#)].
- [25] S. Alekhin, J. Blümlein, and S. Moch, *Strange sea determination from collider data*, Phys. Lett. B **777** (2018) 134–140, [[arXiv:1708.01067](#)].
- [26] A. Cooper-Sarkar and K. Wichmann, *QCD analysis of the ATLAS and CMS W^\pm and Z cross-section measurements and implications for the strange sea density*, Phys. Rev. D **98** (2018), no. 1 014027, [[arXiv:1803.00968](#)].
- [27] **NNPDF** Collaboration, R. D. Ball, S. Carrazza, L. Del Debbio, S. Forte, Z. Kassabov, J. Rojo, E. Slade, and M. Ubiali, *Precision determination of the strong coupling constant within a global PDF analysis*, Eur. Phys. J. **C78** (2018), no. 5 408, [[arXiv:1802.03398](#)].
- [28] **CDF** Collaboration, T. A. Aaltonen et al., *Measurement of $d\sigma/dy$ of Drell-Yan e^+e^- pairs in the Z Mass Region from $p\bar{p}$ Collisions at $\sqrt{s} = 1.96$ TeV*, Phys. Lett. **B692** (2010) 232–239, [[arXiv:0908.3914](#)].
- [29] **D0** Collaboration, V. M. Abazov et al., *Measurement of the shape of the boson rapidity distribution for $p\bar{p} \rightarrow Z/\gamma^* \rightarrow e^+e^- + X$ events produced at $\sqrt{s}=1.96$ -TeV*, Phys. Rev. **D76** (2007) 012003, [[hep-ex/0702025](#)].
- [30] **ATLAS** Collaboration, G. Aad et al., *Measurement of the inclusive W^\pm and Z/γ^* cross sections in the electron and muon decay channels in pp collisions at $\sqrt{s} = 7$ TeV with the ATLAS detector*, Phys.Rev. **D85** (2012) 072004, [[arXiv:1109.5141](#)].
- [31] **CMS** Collaboration, V. Khachatryan et al., *Measurement of the differential cross section and charge asymmetry for inclusive $pp \rightarrow W^\pm + X$ production at $\sqrt{s} = 8$ TeV*, Eur. Phys. J. **C76** (2016), no. 8 469, [[arXiv:1603.01803](#)].
- [32] V. Bertone, S. Carrazza, and J. Rojo, *APFEL: A PDF Evolution Library with QED corrections*, Comput.Phys.Commun. **185** (2014) 1647, [[arXiv:1310.1394](#)].
- [33] J. Gao, *Massive charged-current coefficient functions in deep-inelastic scattering at NNLO and impact on strange-quark distributions*, JHEP **02** (2018) 026, [[arXiv:1710.04258](#)].

- [34] E. L. Berger, J. Gao, C. S. Li, Z. L. Liu, and H. X. Zhu, *Charm-Quark Production in Deep-Inelastic Neutrino Scattering at Next-to-Next-to-Leading Order in QCD*, Phys. Rev. Lett. **116** (2016), no. 21 212002, [[arXiv:1601.05430](#)].
- [35] S. Forte, E. Laenen, P. Nason, and J. Rojo, *Heavy quarks in deep-inelastic scattering*, Nucl. Phys. **B834** (2010) 116–162, [[arXiv:1001.2312](#)].
- [36] **The NNPDF** Collaboration, R. D. Ball et al., *Impact of Heavy Quark Masses on Parton Distributions and LHC Phenomenology*, Nucl. Phys. **B849** (2011) 296, [[arXiv:1101.1300](#)].
- [37] R. Boughezal, J. M. Campbell, R. K. Ellis, C. Focke, W. Giele, X. Liu, F. Petriello, and C. Williams, *Color singlet production at NNLO in MCFM*, Eur. Phys. J. C **77** (2017), no. 1 7, [[arXiv:1605.08011](#)].
- [38] T. Carli et al., *A posteriori inclusion of parton density functions in NLO QCD final-state calculations at hadron colliders: The APPLGRID Project*, Eur.Phys.J. **C66** (2010) 503, [[arXiv:0911.2985](#)].
- [39] R. Gavin, Y. Li, F. Petriello, and S. Quackenbush, *FEWZ 2.0: A code for hadronic Z production at next-to-next-to-leading order*, Comput. Phys. Commun. **182** (2011) 2388–2403, [[arXiv:1011.3540](#)].
- [40] R. Boughezal, C. Focke, X. Liu, and F. Petriello, *W-boson production in association with a jet at next-to-next-to-leading order in perturbative QCD*, Phys. Rev. Lett. **115** (2015), no. 6 062002, [[arXiv:1504.02131](#)].
- [41] A. Gehrmann-De Ridder, T. Gehrmann, E. W. N. Glover, A. Huss, and T. A. Morgan, *Precise QCD predictions for the production of a Z boson in association with a hadronic jet*, Phys. Rev. Lett. **117** (2016), no. 2 022001, [[arXiv:1507.02850](#)].
- [42] M. Czakon, A. Mitov, M. Pellen, and R. Poncelet, *NNLO QCD predictions for W+c-jet production at the LHC*, [arXiv:2011.01011](#).
- [43] **NNPDF** Collaboration, R. Abdul Khalek et al., *Parton Distributions with Theory Uncertainties: General Formalism and First Phenomenological Studies*, Eur. Phys. J. C **79** (2019), no. 11 931, [[arXiv:1906.10698](#)].
- [44] **NNPDF** Collaboration, R. Abdul Khalek et al., *A first determination of parton distributions with theoretical uncertainties*, Eur. Phys. J. C (2019) 79:838, [[arXiv:1905.04311](#)].
- [45] **NNPDF** Collaboration, R. D. Ball, E. R. Nocera, and R. L. Pearson, *Nuclear Uncertainties in the Determination of Proton PDFs*, Eur. Phys. J. **C79** (2019), no. 3 282, [[arXiv:1812.09074](#)].
- [46] R. Abdul Khalek, J. J. Ethier, J. Rojo, and G. van Weelden, *nNNPDF2.0: quark flavor separation in nuclei from LHC data*, JHEP **09** (2020) 183, [[arXiv:2006.14629](#)].
- [47] **NNPDF** Collaboration, R. D. Ball et al., *Parton distributions for the LHC Run II*, JHEP **04** (2015) 040, [[arXiv:1410.8849](#)].
- [48] R. D. Ball, V. Bertone, F. Cerutti, L. Del Debbio, S. Forte, et al., *Reweighting and Unweighting of Parton Distributions and the LHC W lepton asymmetry data*, Nucl.Phys. **B855** (2012) 608–638, [[arXiv:1108.1758](#)].

- [49] **The NNPDF** Collaboration, R. D. Ball et al., *Reweighting NNPDFs: the W lepton asymmetry*, Nucl. Phys. **B849** (2011) 112–143, [[arXiv:1012.0836](#)].
- [50] E. R. Nocera, M. Ubiali, and C. Voisey, *Single Top Production in PDF fits*, JHEP **05** (2020) 067, [[arXiv:1912.09543](#)].
- [51] L. A. Harland-Lang, A. D. Martin, P. Motylinski, and R. S. Thorne, *Parton distributions in the LHC era: MMHT 2014 PDFs*, Eur. Phys. J. **C75** (2015) 204, [[arXiv:1412.3989](#)].
- [52] S. Alekhin, J. Blümlein, S. Moch, and R. Placakyte, *Parton distribution functions, α_s , and heavy-quark masses for LHC Run II*, Phys. Rev. **D96** (2017), no. 1 014011, [[arXiv:1701.05838](#)].
- [53] **NNPDF** Collaboration, R. D. Ball, V. Bertone, M. Bonvini, S. Carrazza, S. Forte, A. Guffanti, N. P. Hartland, J. Rojo, and L. Rottoli, *A Determination of the Charm Content of the Proton*, Eur. Phys. J. **C76** (2016), no. 11 647, [[arXiv:1605.06515](#)].
- [54] S. Alekhin et al., *HERAFitter*, Eur. Phys. J. **C75** (2015), no. 7 304, [[arXiv:1410.4412](#)].
- [55] A. Buckley, J. Ferrando, S. Lloyd, K. Nordström, B. Page, et al., *LHAPDF6: parton density access in the LHC precision era*, Eur.Phys.J. **C75** (2015) 132, [[arXiv:1412.7420](#)].
- [56] K. J. Eskola, P. Paakkinen, H. Paukkunen, and C. A. Salgado, *EPPS16: Nuclear parton distributions with LHC data*, Eur. Phys. J. C **77** (2017), no. 3 163, [[arXiv:1612.05741](#)].
- [57] A. Kusina et al., *Impact of LHC vector boson production in heavy ion collisions on strange PDFs*, [arXiv:2007.09100](#).
- [58] **HERMES** Collaboration, A. Airapetian et al., *Reevaluation of the parton distribution of strange quarks in the nucleon*, Phys. Rev. **D89** (2014), no. 9 097101, [[arXiv:1312.7028](#)].
- [59] I. Borsa, R. Sassot, and M. Stratmann, *Probing the Sea Quark Content of the Proton with One-Particle-Inclusive Processes*, Phys. Rev. **D96** (2017), no. 9 094020, [[arXiv:1708.01630](#)].
- [60] **JAM** Collaboration, N. Sato, C. Andres, J. Ethier, and W. Melnitchouk, *Strange quark suppression from a simultaneous Monte Carlo analysis of parton distributions and fragmentation functions*, Phys. Rev. D **101** (2020), no. 7 074020, [[arXiv:1905.03788](#)].